High-throughput analysis of the ideality factor to evaluate the outdoor performance of perovskite solar minimodules

Esteban Velilla[1,2], Franklin Jaramillo[1*], Iván Mora-Seró[2*]

[1] Centro de Investigación, Innovación y Desarrollo de Materiales – CIDEMAT, Universidad de Antioquia UdeA, Calle 70 No. 52-21, Medellín, Colombia

[2] Institute of Advanced Materials (INAM), Universitat Jaume I, Av. de Vicent Sos Baynat, s/n 12006 Castelló de la Plana, Spain

[*] Corresponding Author: franklin.jaramillo@udea.edu.co, sero@uji.es

Halide perovskite solar cells (PSCs) exhibit a unique combination of properties, including ion migration, low nonradiative recombination and low performance dependence on temperature. Because of these idiosyncrasies, it is debatable whether standard procedures for assessing photovoltaic technologies are sufficient to appropriately evaluate this technology. Here, we show a low dependence of the open-circuit voltage on the temperature of a $MAPbI_3$ minimodule that allows a high-throughput outdoor analysis based on the ideality factor (n_{ID}). Accordingly, three representative power loss tendencies obtained from I-V curves measured with standard procedures are compared with their corresponding n_{ID} patterns under outdoor conditions. Therefore, based on the linear relationship between T_{80} and the time to reach n_{ID}=2 (T_{nID2}) is demonstrate that n_{ID} analysis could offer important complementary information with important implications for the outdoor development of this technology, providing physical insight into the recombination mechanism dominating the performance, improving the understanding of the degradation processes and device characterization.

To evaluate the lifetime of a photovoltaic device, a parameter that refers to the time at which the device reaches 80% of its initial rated power (T_{80}) is commonly used as a figure of merit. T_{80} depends on various factors, such as the materials and procedures used for device fabrication, cell interconnects, weather conditions, seasonal variations, installation conditions, shading and soiling effects, and electrical mismatch between cells[1]. This parameter is commonly obtained from the relationship between the maximum power and time in a long-term analysis of a device under real outdoor operating conditions. Moreover, considering that the performance over time shows seasonal behavior and a

gradual performance loss tendency, T_{80} has been commonly fitted using statistical methods, such as linear regression, to estimate the degradation rate[2]. However, in the case of emerging technologies such as perovskite solar cells (PSCs), most stability studies have focused on small, laboratory-scale devices operating indoors, and few statistical data have been collected under real outdoor operation[3]. Nevertheless, under high-irradiance conditions, PSCs demonstrate significant differences from conventional Si cells, as has been shown for perovskite minimodules operating outdoors[4] and for nonencapsulated solar cells under simulated weather conditions in the laboratory[5]. These results indicate that PSCs show lower correlations of their performance and open-circuit voltage (V_{oc}) with temperature than other commercial technologies, such as silicon[6], for which the deleterious effects of temperature on performance are well known[7,8]. This difference in temperature sensitivity is an important aspect of PSC technology.

PSCs are expected to have a significant impact in the future if they are able to provide significant performance outdoors. Outdoor conditions are highly demanding, as they are characterized by day-night, seasonal and weather cycles that correspond to drastic variations in irradiation, temperature and moisture. While accelerated performance tests are useful for predicting the behavior of devices, continuous outdoor tests are also required to provide information on the applicability of this technology in the real world. The outdoor exploitation of solar devices requires encapsulation to protect the electrodes and active areas of cells against the environment, avoid corrosion processes, increase the electrical insulation to eliminate leakage currents, and provide thermal and mechanical support[9]. In this context, international standards such as IEC 61215 suggest various accelerated tests intended to identify potential failures in silicon photovoltaic modules (broken interconnects, cracked cells, delamination, dielectric breakdown, bypassed diodes and corrosion). Thus, based on the experience gained in recent decades through such accelerated tests and field evaluations, these failures in photovoltaic modules have been correlated with various degradation modes, such as corrosion, delamination, discoloration, glass breakage, cell cracking, potential-induced degradation, current leakage, ion migration, hot spots, and soiling[10,11]. Nevertheless, because the standards do not include all possible degradation modes and, in real operation, photovoltaic devices can be affected by different degradation modes simultaneously, it is not always possible to estimate the real lifetime from these tests[12].

In the case of emerging technologies such as PSCs, no international standards have been fully established, and most published works have focused on laboratory-scale cells (i.e., 1 cm^2 or smaller in size); consequently, various methods and materials have been used to evaluate the stability and degradation performance of these technologies[5,13–17]. In this regard, a broadly supported consensus

statement on reporting data related to stability assessment was recently published, highlighting certain particularities of PSC technology that must be taken into account[18]. For instance, in contrast to mature photovoltaic technologies such as Si and GaAs, PSCs show performance loss reversibility under day-night cycles[19,20]; a hysteresis effect in the current-voltage (I-V) curves, which could induce errors in performance determination[21]; and a lower dependence of performance and V_{oc} on temperature[22]. Nevertheless, while these peculiarities of PSCs could be seen as drawbacks for their systematic analysis, they also provide new opportunities for the characterization of PSCs[23]. This technology is in its infancy, and there are few statistical data available for large devices operated outdoors[3]. Therefore, insufficient data are available to fully establish or identify the degradation modes and mechanisms of PSCs and their impact on outdoor performance evolution.

Conventionally, the evolution of solar cell device performance is monitored through the systematic measurement of I-V curves considering the temperature and illumination conditions. In the laboratory, it is relatively easy to set up tests to track the performance at the maximum power point; however, such control is intrinsically unreasonable outdoors. The illumination and temperature variations induced by day-night, seasonal and weather conditions necessitate a systematic analysis of a high quantity of data, depending on the measurement sampling rate and exposure time[24]. Hence, in such power loss studies, it is common to correct for temperature and irradiance in the I-V curves in accordance with the standard test conditions (STC, corresponding to an irradiance of 1000 W/m^2 and a module temperature of 25 °C). However, such conditions are difficult to reach outdoors[25]. In addition, although the conventional method of monitoring outdoor module performance based on I-V curves produces rich numerical data, it offers no direct indication of the physical processes occurring in the device and thus provides no information about degradation process.

In this context, ideality factor, n_{ID}, also called the quality factor or shape curve factor has been used to define the electrical behavior of solar devices due to its relationship with conduction, transport, recombination and behavior at interface junctions, providing direct information on the dominating recombination processes. Therefore, in silicon, n_{ID} has been widely studied and estimated in various ways, such as using the relationship between the open-circuit voltage (V_{oc}) and light intensity (see Eq. (1)) to overcome the effects of series resistance[27], performing numerical calculations[28], and extracting this parameter from I-V curves at different light intensities and temperatures using equivalent circuit models[29]. For PSCs, although there are relatively few reports related to this parameter, Tress and coworkers have reported a full interpretation of n_{ID} for nonencapsulated cells, establishing the relationship between the dominating recombination process, the light intensity and V_{oc}[26]. In addition, n_{ID} has been estimated through impedance/frequency-response (IFR) analysis[30–32], from the I-V curve

at standard test conditions using an one-diode model[33], and from the dark I-V curve through numerical simulation considering the continuity and Poisson's equations[34]. Moreover, agreement has been shown between the n_{ID} value estimated from the recombination resistance extracted through IFR analysis and the value calculated from V_{oc} at different light intensities [31,32].

$$e \cdot V_{OC} = m \cdot E_g + n_{ID} \cdot k_B \cdot T \cdot m \cdot ln\frac{G}{G_0} \qquad (1)$$

where e is the electron charge, m is the number of identical cells connected in series, E_g is the light absorber bandgap, k_B is the Boltzmann constant, T is the temperature, G is the irradiance and G_0 is a constant with the same units as G.

Here, all of these considerations and the current state of PSC technology motivate us to explore new characterization methodologies that do not merely determine the degradation loss but also provide an understanding of the degradation modes and mechanisms involved[35]. Specifically, it is of interest to take advantage of the properties of perovskite materials and perform evaluations following the common standards and new evaluations developed especially for PSCs to create a better understanding of the real behavior outdoors, including the behavior of larger devices such as minimodules or modules. In this context, despite the potential of n_{ID}, this parameter has not been employed to monitor device evolution over time to see how the relevant processes evolve, for example, in the case of degradation. Therefore, we propose to take advantage of the weak dependence of V_{oc} on T in PSCs[4,5,22] to calculate n_{ID} and use it as a figure of merit for monitoring and characterizing the outdoor performance of this technology. In this way, day-night cycles, including dawn and noon conditions, can naturally provide a broad range of illumination conditions, allowing n_{ID} to be determined. Moreover, we can take advantage of this interesting parameter to determine the physical processes acting on devices in order to link them with the degradation modes. For this purpose, we tracked outdoor $MAPbI_3$ minimodules and recorded the evolution of the maximum power (P_{max}) under power rating conditions suggested by the IEC61853-1 standard, specifically the nominal operating cell temperature (NOCT) conditions, to compare the resulting data with the n_{ID} evolution estimated using **Eq. (1).** We show that this new methodology identifies features similar to those found using the classical approach based on P_{max}, enabling tracking of the physical processes occurring in the device. Finally, we show a linear relationship between the time at which the module reaches n_{ID} = 2 (Tn_{ID2}) and T_{80}, suggesting the complementarity of these two parameters. This complementarity has important implications for improving the characterization and understanding of degradation processes and, consequently, for the outdoor optimization of PSCs.

Evaluation of the device outdoor performance

$MAPbI_3$ minimodules of 8.0 cm^2 in size formed of m=4 cells interconnected in series, with a mesoporous inverted structure (NiO_x/Al_2O_3/$MAPbI_3$/PCMB/rhodamine/Au), were fabricated on ITO substrates of 5 x 5 cm in a drybox by spin coating[36] (see **Fig. 1a-b, Supplementary Figure 1** and the Methods section). The devices were manually encapsulated with ethylene vinyl acetate (EVA). Different batches of encapsulated minimodules with different performances were exposed to natural sunlight, without a tracker, in the facilities of the Solar Cell Outdoor Performance Laboratory of the University of Antioquia (OPSUA) in Medellín, Colombia, during January-June 2019 (see **Fig. 1c** and **Supplementary Figure 2**). Regarding full outdoor performance tests, it is worth remarking that the IEC 61853-1 international standard allows the evaluation of different solar technologies based on different power ratings, accounting for irradiance and temperature, to determine the impact of weather variables on performance[37], while the ISOS-O-2 protocol is intended to evaluate the P_{max} stability of devices[38]. In this sense, both protocols are compatible and complementary, and both are based on data extracted from the I-V curve. Therefore, weather variables such as irradiance and ambient temperature (T) as well as the I-V curves of the devices were registered and stored every minute during daylight hours (5:30 AM to 6:30 PM) using a previously developed monitoring system[25]. To ensure a full I-V curve, V_{oc} was measured and recorded before any other measurement, and the curve was subsequently scanned between -0.5 V and 1.1·V_{oc} in the forward direction. After scanning, the I-V tracer was disconnected, and the device was in the open-circuit condition.

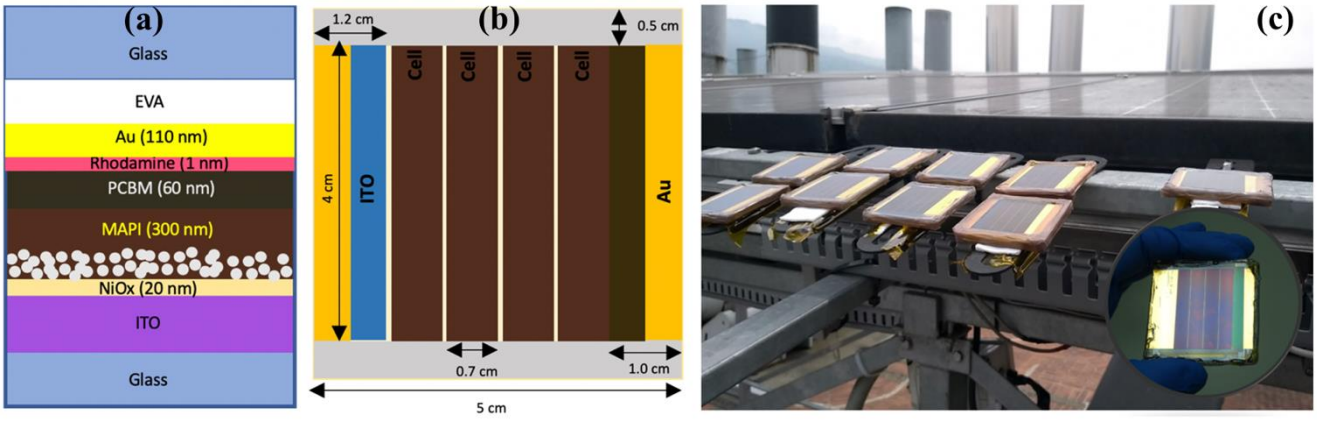

Fig. 1 | Configuration and outdoor placement of $MAPbI_3$ minimodules. **(a)** Configuration of the inverted-structure $MAPbI_3$ minimodules characterized in this work. **(b)** Minimodule scheme design. The gray region corresponds to the laser etching performed to limit the active area; the blue region corresponds to the dead area where scribe lines were created (P1, P2 and P3); the brown regions

represent the active areas of the 4 cells; and the dark brown, beige and orange regions correspond to the contact electrodes. **(c)** Photograph of installed PSC minimodules at the facilities of the Solar Cell Outdoor Performance Laboratory of the University of Antioquia (OPSUA) in Medellín, Colombia. One of the evaluated minimodules is shown in the inset photograph.

The collected high-throughput outdoor data were processed in accordance with the flowchart shown in **Supplementary Figure 3** to evaluate the performance; see **Supplementary Note 1 and Note 2**. In brief, from the I-V curves, photovoltaic parameters such as V_{oc}, the short-circuit current (I_{sc}), the fill factor (FF), the photoconversion efficiency and P_{max} were extracted. In addition, the irradiances and ambient temperatures were also recorded during I-V measurement (synchronously). Subsequently, the raw data were filtered based on the linearity determination criterion to minimize transient effects related to changes in irradiance, shadowing caused by clouds or droplets, or atypical data[4] (**Supplementary Figure 4a**). Therefore, a high-throughput set of data was obtained to estimate the outdoor performance (see **Fig. 2**). Moreover, the power loss tendency or degradation shape was obtained by calculating the outdoor performance observed in the measurement sets, each of which contained measurements recorded over 100 hours of outdoor exposure (see **Fig. 3a-c**). The data in each set were filtered considering a deviation of 5% from the irradiance levels corresponding to the power rating conditions indicated by IEC 61853-1[37], that is, 1000 W/m^2, corresponding to standard test conditions (STC); 800 W/m^2, corresponding to NOCT conditions; 500 W/m^2, corresponding to low-temperature conditions; and 200 W/m^2, corresponding to low-irradiance conditions. The period of time considered to estimate the average outdoor performance was slightly longer than four days (100 h), which is long enough to consider the data recorded in each set to be statistically valid, allowing the calculation of reliable average values for tracking the performance evolution.

From the analyzed outdoor samples, three different P_{max} evolution patterns over time can be distinguished, named convex, linear and concave patterns because of the shapes they exhibit (see **Fig. 3a-c**). See **Supplementary Figure 5-8** for a further analysis of each behavior pattern. These three distinctive patterns are commonly described for degradation processes in the literature in order to study possible degradation paths and estimate the failure time[39].

Fig. 2 shows the data collected during only the first 100 h of outdoor operation of representative devices of each pattern. The corresponding maps show the average impact of weather variables on P_{max}, V_{oc}, and I_{sc} over a broad set of T values and irradiances, ranging between 18 and 42 °C and up to 1200 W/m^2, respectively. These ranges correspond to the most representative values of the weather

variables and performances recorded during the time window considered (**Supplementary Figure 2j-l**).

Fig. 2 allows us to identify some trends, such as the low temperature dependence of V_{oc}. In this regard, the data related to the convex pattern (**Fig. 2a,d,g**) and the linear pattern (**Fig. 2b,e,h**) follow the expected trend, with P_{max}, I_{sc} and V_{oc} increasing with increasing irradiance but showing only a low sensitivity to temperature. In contrast, the data related to the concave pattern sample do not exhibit this monotonic variation, instead showing local maxima or minima at various irradiance levels and temperatures (**Fig. 2c,f,i**). Moreover, when a lower total sampling time of 50 h is considered, the T_{80} of this sample is estimated to be 80 h (**Supplementary Figure 8g**), indicating that during the first 100 h of exposure, fast degradation occurs, causing the nonmonotonic behavior depicted in **Fig. 2c,f,i**.

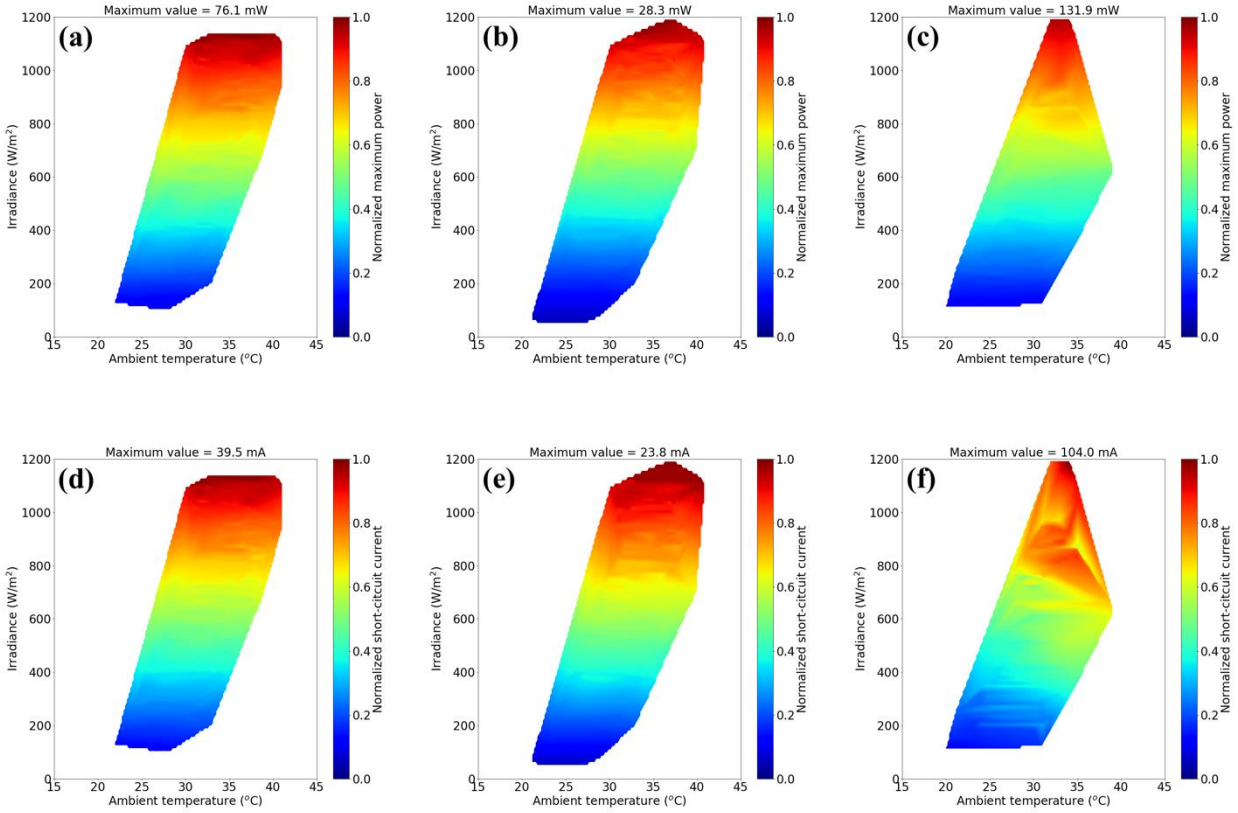

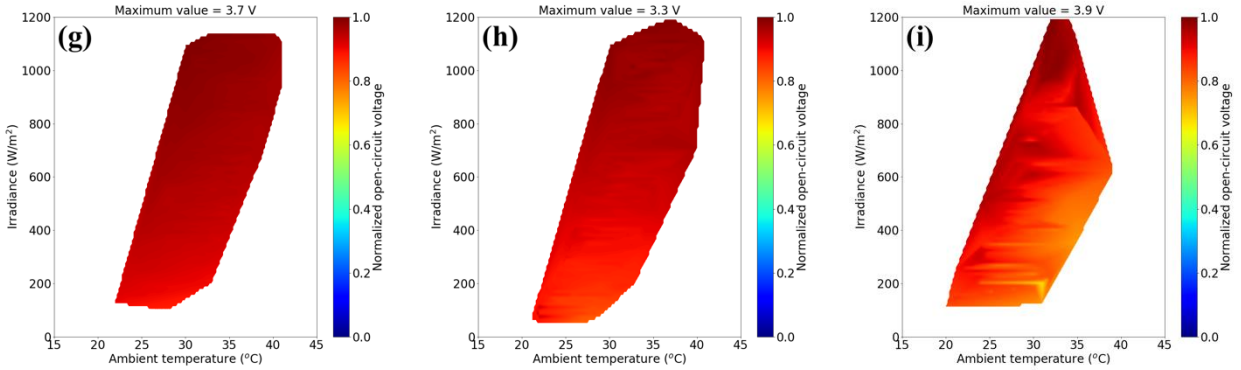

Fig. 2 | Normalized outdoor performance of three representative PSC samples during the first 100 hours of exposure. (a-c) Maximum power; these data are also used for the calculation of the first point values for 100 h of exposition time plotted in **Fig. 3a-c**. **(d-f)** Short-circuit current. **(g-i)** Open-circuit voltage. Panels **(a)**, **(d)** and **(g)** correspond to a device with a convex P_{max} shape, according to **Fig. 3a**. Panels **(b)**, **(e)**, and **(h)** correspond to a device with a linear P_{max} shape, according to **Fig. 3b**. Finally, panels **(c)**, **(f)**, and **(i)** correspond to a device with a concave P_{max} shape, according to **Fig. 3c**. The color bar indicates the variable range. At the top of each plot, the maximum recorded value used to normalize the data for each variable is shown.

Although all of the minimodules were fabricated and monitored in a similar way and exposed to similar outdoor conditions (**Supplementary Figure 2**), a broad range of behaviors is observed, which appears to be mainly related to the manual encapsulation method employed (**Supplementary Figure 5**). This fact allows us to check the methodology proposed here over a broad range of behaviors, as these three different P_{max} patterns have all been previously observed for PSCs[40], consequently showing the generality of the approach. For instance, the convex pattern has been observed for encapsulated PSCs stored at room temperature, for which the P_{max} loss was attributed to interface deterioration inducing interfacial recombination, along with perovskite layer degradation related to the formation of deeper defect states[41]. The linear and convex patterns have both previously been observed in nonencapsulated cells under controlled relative humidity conditions, depending on the PbI_2/MAI ratio[42], while the concave pattern has been observed in encapsulated cells exposed to different levels of sunlight, suggesting that light intensity is the main variable that accelerates the degradation process[14]. In addition, this shape has also been observed in nonencapsulated PSCs under different atmospheres and light intensities, with faster degradation under higher relative humidity[16], and in nonencapsulated devices tested under air exposure, suggesting an increase in electrical traps due to ion migration from the perovskite layer to other layers as the main reason for the degradation[43]. It is worth noting that in

these cases, the controlled atmospheres enabled correlation with the physical origins of the degradation, whereas under outdoor conditions, because various factors may be involved in the degradation process, determining the physical origin of the degradation is not always possible.

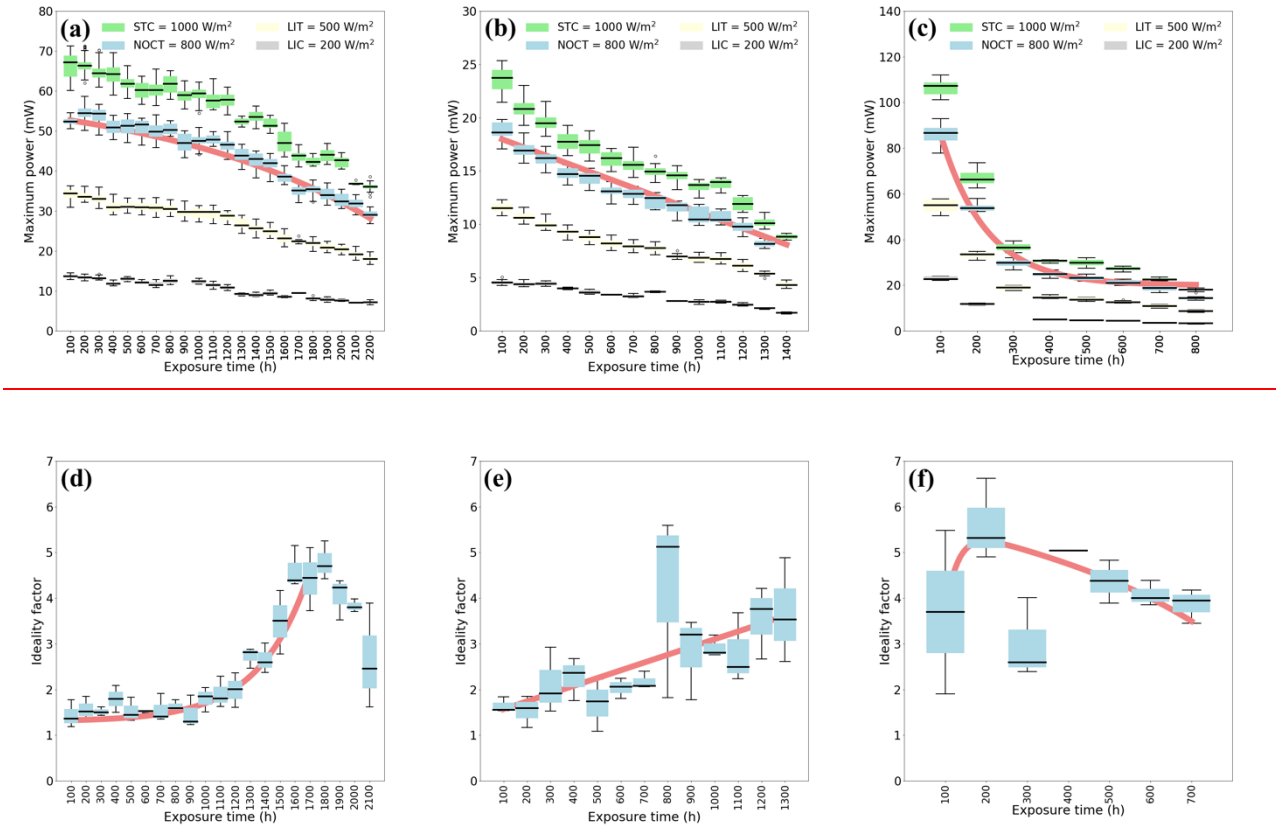

Fig. 3 | Patterns of degradation in the maximum power and the ideality factor. (a-c) Maximum power under different power rating conditions suggested by IEC 61863 for the convex, linear and concave patterns. Green boxes correspond to 1000 W/m^2 (STC), blue boxes correspond to 800 W/m^2 (NOCT), yellow boxes correspond to 500 W/m^2 (low-temperature condition) and gray boxes correspond to 200 W/m^2 (low-irradiance condition) for the **(a)** convex, **(b)** linear and **(c)** concave degradation behaviors. **(d-f)** Ideality factor analysis of the same samples: **(d)** n_{ID} exhibits a concave pattern for samples exhibiting a convex P_{max} pattern, **(e)** n_{ID} exhibits a linear pattern for samples exhibiting a linear P_{max} pattern, and **(f)** n_{ID} exhibits a convex pattern for samples exhibiting a concave P_{max} pattern. The average n_{ID} was calculated using all data points recorded during each 100 h period (**Supplementary Figure 3** and **Figure 9**). The boxplots were estimated by calculating n_{ID}, filtering the data by T between 25 and 37 °C in steps of 2 °C with a deviation of $\pm$1 °C, and obtaining the maximum and minimum n_{ID} to define the upper and lower bars, respectively. The thick black line on each box represents the average performance in the corresponding time window. The boxplots were

obtained by calculating the variables observed in the measurement sets, each of which contained measurements recorded over 100 hours of outdoor exposure. Moreover, in all cases, a red ~~dotted~~ line is included for the NOCT P_{max} data and the n_{ID} data as a visual guide to illustrate the shapes related to the convex, linear and concave patterns.

Evolution of the ideality factor of outdoor-exposed devices

Considering the low dependence of the performance of PSCs on T, as observed in the literature[4,5] and confirmed by the maps of our data in **Fig. 2** and **Fig. 3**, n_{ID} can be considered a good parameter for monitoring the outdoor evolution of this technology. While taking advantage of the different levels of illumination caused by day-night cycles to collect a large amount of data across a broad range of illumination conditions, n_{ID} can be calculated to provide information on the physical processes occurring during the exposure. Accordingly, the average n_{ID} values were calculated using **Eq. (1)** while considering the different measurements of V_{oc} recorded at different irradiance levels in every 100 hours of the high-throughput data (**Supplementary Figure 9**). The results are shown in **Fig. 3d-f** in the form of boxplots to illustrate the deviations from the average value due to temperature changes. n_{ID} also exhibits three distinct evolution patterns or shapes, pointing to a direct relation and complementarity with P_{max}. Specifically, a convex P_{max} evolution pattern corresponds to a concave n_{ID} evolution pattern (**Fig. 3a,d**) and *vice versa* (**Fig. 3c,f**), while for a linear P_{max} pattern, a linear n_{ID} pattern is observed (**Fig. 3b,e**).

In the cases of convex P_{max}/concave n_{ID} patterns (see **Fig. 3a,d**) and linear patterns (**Fig. 3b,e**), at times earlier than T_{80} (1442.2 and 414.2 h, respectively; see **Supplementary Figure 5**), n_{ID} takes values between 1 and 2, indicating bulk Shockley-Read-Hall (SRH) recombination[26], which is characteristic of most PSCs. After longer times, n_{ID} exhibits values above 2, characteristic of a multiple-trap distribution, originating from the formation of trap states, causing the performance degradation, as pointed out by Khadka et al.[41]. In the case of concave P_{max}/convex n_{ID} patterns (**Fig. 3e,f**), the initial values of n_{ID} are higher than 2, indicating fast degradation in the first 100 h of exposure due to the formation of multiple trap states. Interestingly, after the initial increase in n_{ID}, a progressive decrease is observed in the concave (**Fig. 3d**) and convex (**Fig. 3f**) cases, suggesting an evolution from bulk recombination to interfacial recombination characterized by a low V_{oc}. Note that this behavior does not imply a recovery in device performance; it only indicates a transition between two different

recombination regimes in the degradation process, from multiple-trap recombination to a regime with higher interfacial recombination.

All of the analyzed minimodules (**Supplementary Figure 5a**) exhibit behavior that can be statistically associated with one of these three patterns (**Supplementary Figure 5b**). Moreover, the samples analyzed here show different degradation rates (**Supplementary Figure 5c**), with a relatively low degradation rate of the initial P_{max} of 0.29%/day for the convex data, a moderate degradation rate of 1.39%/day for the linear data, and a faster degradation rate of 7.68%/day for the concave data. The faster power loss observed for samples with concave P_{max}/convex n_{ID} patterns can be associated with failures of the encapsulation that allowed moisture ingress, bleaching the perovskite to a yellow-white color[16]; see **Supplementary Figure 2d-i** and **Figure 10** for outdoor and indoor examples, respectively. Similarly, a rapid power drop, within less than 5 days, has also been observed in encapsulated perovskite minimodules under outdoor conditions due to a breach of the edge sealant that allowed water ingress, along with the associated color change[44]. For devices exhibiting convex P_{max}/concave n_{ID} data or linear data, there was no evidence of color change even after more than 900 hours of exposure; nevertheless, they also degraded, indicating another kind of degradation mechanism (**Supplementary Figure 2a-b**). Note that encapsulation protects against not only moisture ingress but also degradation originating from the release of organic components of $MAPbI_3$ into the atmosphere. Different $MAPbI_3$ degradation reactions result in the formation of a PbI_2 solid and NH_2CH_3, HI, NH_3, CH_3I[45,46], or I_2 gases[47]. Correspondingly, samples exhibiting convex P_{max}/concave n_{ID} or linear patterns show different degradation rates that can be associated with differences in the quality of the encapsulation process. During the first stage (when n_{ID}<2), the samples undergo SRH recombination dominated by lead vacancies and interstitial halogen[47]. However, the formation of different types of gases leads to the appearance of multiple trap states, causing n_{ID} to become higher than 2. These gases can be released into the atmosphere through small pores formed during the preparation of the encapsulant or produced by its degradation. Convex P_{max}/concave n_{ID} patterns could be indicative of the latter case, where the rate of degradation increases after a certain time (**Supplementary Figure 5c**).

The method used for n_{ID} determination has been verified through indoor measurements. In indoor tests, excellent agreement between the n_{ID} values estimated from V_{oc}-*light intensity* data and the results of IFR analysis has been observed[31,32]. Thus, the methodology applied to obtain n_{ID} can be validated by comparing the values obtained from the analysis of V_{oc} *vs.* G using **Eq. (1)** with the results of an independent additional calculation of n_{ID}. **Fig. 4a** shows the n_{ID} values calculated by fitting the V_{oc} data collected at different light intensities using **Eq. (1)**. n_{ID} takes values close to 1.6 for a fresh device and higher than 3 for a device after a long period of outdoor testing. Impedance spectra were

independently measured under different light intensities to calculate the recombination resistance[30,32,49], R_{rec}, considering negligible transport and charge transfer resistances in both the bulk and the contact layers and at interfaces[48]. In this case, n_{ID} can be calculated from the slope of the logarithmic plot of R_{rec} *vs.* V_{oc} [30,32,49]. The IFR data at different intensities (see **Fig. 4b** and **Supplementary Figure 12**) were fitted to the equivalent circuit shown in **Supplementary Figure 13** to obtain R_{rec}:

$$R_{rec} = R_{00} e^{\left(\frac{-q \cdot V}{n_{ID} \cdot k_B \cdot T}\right)} \qquad (2)$$

where R_{00} is an independent parameter expressed in units of resistance. The n_{ID} values calculated using **Eq. (2)** (see **Fig. 4c**) show excellent agreement with the n_{ID} values calculated using **Eq. (1)**, validating the calculation of n_{ID} from V_{oc} *vs. G* data collected outdoors (**Supplementary Figure 9**).

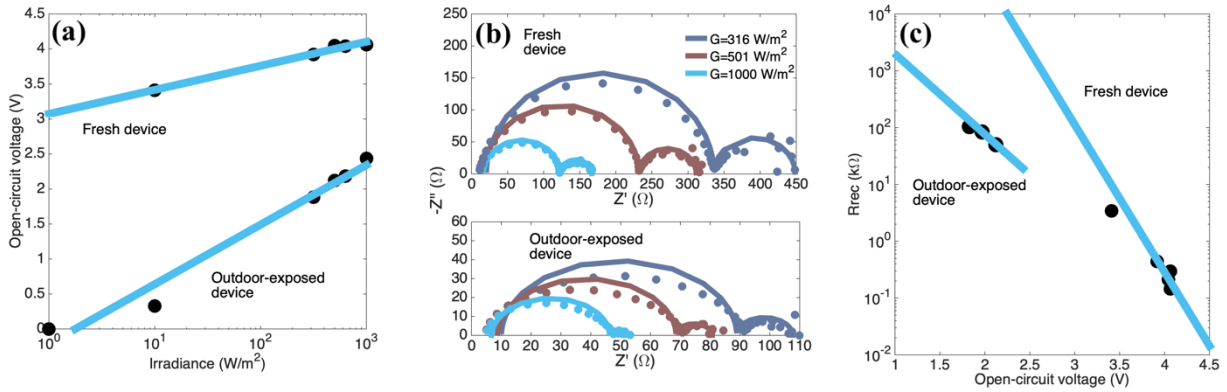

Fig. 4 | Ideality factor under indoor conditions. (a) Calculation of n_{ID} from the relationship between the open-circuit voltage and the irradiance level, where the blue lines correspond to fits in accordance with **Eq. (1)**. These data indicate that n_{ID} = 1.6 for the fresh device and 3.5 for the outdoor-exposed device. **(b)** Nyquist diagrams of impedance at different light intensities (experimental data, plotted as dots) and their corresponding fits (plotted as solid lines) for a fresh device (upper plot) and an outdoor-exposed device (lower plot). The fits correspond to the best solutions obtained by using a genetic algorithm combined with the simplex method to minimize the error between the experimental data and the circuit model (**Supplementary Figure 13**), according to **Eq. (3)**. The calculated parameters from the IFR fitting analysis are shown in **Supplementary Table 4** for the fresh device and in **Supplementary Table 5** for the outdoor-exposed device. **(c)** Calculation of n_{ID} from the relationship between R_{rec} and V_{oc} using **Eq. (2)**. The linear regression fits indicate that n_{ID} = 1.5 for the fresh device and 3.4 for outdoor-exposed device. The measurements were carried out at room temperature (25°C).

Moreover, this comparative analysis also highlights the relationship between n_{ID} and R_{rec} related to recombination processes. To this end, **Supplementary Figure 15** shows the results of simultaneously monitoring P_{max}, n_{ID} and R_{rec}, from which it can be observed that P_{max} exhibits monotonic behavior, while n_{ID} and R_{rec} show similar and richer patterns that allow the changes in the recombination mechanism to be tracked more directly than can be achieved with P_{max}. These observations illustrate the valuable complementarity that the determination of n_{ID} can provide for the study and understanding of outdoor PSC tests. This approach can be employed as a diagnostic tool to detect initial failures or validate the status of devices.

Relationship between n_{ID} and T_{80}

T_{80} is an extensively used parameter in the photovoltaic industry[1,2]. This parameter can be calculated from the power loss tendency depicted by the boxplots for the different PRCs cases considered in **Fig. 3a-c**. Because the NOCT conditions are considered the most representative power rating conditions for outdoor operation[25] and NOCT performance is included on the datasheets for commercial solar modules, we normalized the average P_{max} under NOCT conditions with respect to the average value obtained for each sample during the first 100 hours of outdoor exposure in order to determine T_{80} (see **Fig. 5a**)**.** Using the samples characterized in **Fig. 2** and **Fig. 3** as representative examples, it is observed that the sample with the concave shape degrades faster (T_{80}=80 h) than the sample with the linear pattern (T_{80}=414.2 h), while the one with the convex pattern shows the slowest degradation rate (T_{80}=1442.2 h). The degradation in P_{max} can be mainly attributed to the decreases in V_{oc} and I_{sc} for the convex and linear patterns, respectively, while for the concave pattern, both of these parameters are significantly degraded (**Supplementary Fig. 6-8**). T_{80} can be obtained directly from the normalized power loss tendency (see **Fig. 5a**).

A complementary analysis to the P_{max} methodology can be performed by considering the average n_{ID} values over time (see **Fig. 3c-e**) and defining Tn_{ID2} as the time in which the value of n_{ID} first reaches 2. In this way, it is possible to observe that for times longer than T_{80} (**Fig. 5a**), n_{ID} exhibits values higher than 2 (**Fig. 5b**). Accordingly, **Fig. 5c** analyzes the relation between Tn_{ID2} and T_{80}, showing a strong linear relationship. This linear relationship indicates that these parameters are correlated and complementary probes of the degradation processes occurring in the devices. T_{80} provides valuable commercial information and a clear idea of a fundamental property of a photovoltaic

module, namely, its lifetime, which is a key concern for the customer. On the other hand, Tn_{ID2} has a physical meaning related to the transition point from bulk SRH recombination through a single level to recombination through multiple levels as a result of device degradation[26]. The linear relationship between these parameters indicates that the degradation processes causing the reduction in device performance, as monitored by T_{80}, manifest as a change in the recombination mechanism, as tracked by T_{nID2}. Accordingly, the complementarity shown in **Fig. 5c** between these two parameters allows us to correlate the commercial parameter with a parameter that has physical meaning. This fact has important implications for the commercial development of perovskite photovoltaics for outdoor applications. Therefore, although it is not possible to extract direct conclusions from T_{80} regarding the degradation mechanisms and how the recombination pathways evolve during the degradation process, it is possible to obtain complementary information from Tn_{ID2} in order to correlate changes in n_{ID} with recombination mechanisms or degradation processes occurring in a device. Establishing this correlation will provide critical complementary insight regarding the fundamental recombination within PSCs, which can be linked to $T_{80.}$ This relationship can then be used to improve the characterization and understanding of the outdoor degradation processes affecting PSC technologies, aid in evaluating other cell configurations and/or encapsulants, and potentially assist in linking outdoor data to indoor tests.

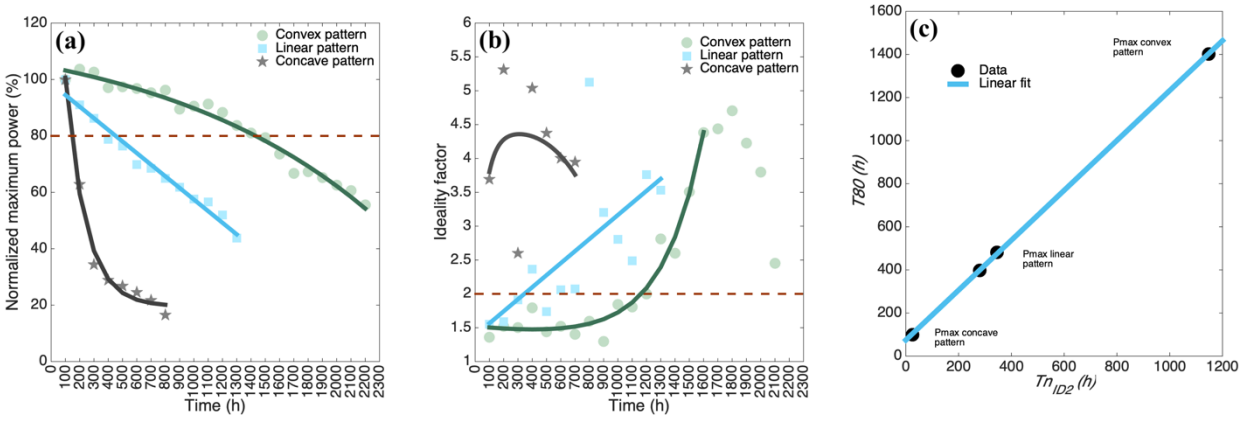

Fig. 5 | Relationship between T_{80} and n_{ID}. (a) Average P_{max} under NOCT conditions for samples normalized with respect to the initial average value during the first 100 h of exposure. The red dashed line corresponds to a 20% loss of power and is used to calculate T_{80}. The symbols represent the normalized average power (see **Fig. 3a-c**) for three samples exhibiting the three different characteristic patterns, and the solid line of each color represents the corresponding fit to the experimental data (**Supplementary Table 3**). **(b)** Ideality factor over time for the samples analyzed in **(a)**. The red dashed line corresponds to n_{ID} = 2 and is used to calculate Tn_{ID2}. The colored markers represent the average n_{ID} values extracted from the experimental data (see **Fig. 3d-f**), and the solid line of each color corresponds

to the fit to the data with the corresponding pattern (**Supplementary Table 3**). **(c)** Relation between the time to reach a 20% power loss (T_{80}) and time to reach an n_{ID} value higher than 2 (Tn_{ID2}). The blue line corresponds to the fit to the data, $T_{80}=1.2Tn_{ID2}+60.1$. In all cases, solid lines correspond to fits, while colored symbols correspond to the estimated data.

Conclusions

This work presents a complementary methodology based on the evaluation of the ideality factor for monitoring the outdoor performance of halide perovskite solar cells, which can improve device characterization under outdoor testing conditions. This methodology takes advantage of the properties of this new class of photovoltaic technology and the direct relationship between n_{ID} and the recombination pathway to provide insight to enable improved data interpretation and understanding of the device degradation processes under outdoor conditions that are relevant to the commercial application of PSCs. By applying this methodology, a high-throughput outdoor performance analysis of $MAPbI_3$ minimodules was carried out following the international standard IEC 61853-1 to evaluate the impact of weather variables on performance. The collected data were processed in measurement sets based on measurements recorded over 100 h of exposure. In each set, n_{ID} was calculated while taking advantage of the different illumination conditions encountered during day-night cycles, and the outdoor performance was calculated based on the NOCT power rating conditions identified in the IEC 61853-1 standard.

Taking advantage of the low dependence of PSCs on temperature, we proposed and then demonstrated an analysis of outdoor performance using n_{ID}. The main advantage of this approach is that it provides direct physical insight related to recombination processes. To this end, we defined Tn_{ID2} as the time at which n_{ID} first reaches a value of 2, with a physical meaning related to the transition point between bulk SRH recombination through a single level to recombination through multiple levels as a result of device degradation[26]. We showed that the three different degradation patterns identified for P_{max} can also be identified by monitoring n_{ID}. In addition, based on the linear relationship between T_{80} and Tn_{ID2}, these two indexes are correlated. Consequently, it is possible to take advantage of their complementarity for the future development of PSCs. While T_{80} provides direct commercial information, namely, the module lifetime, Tn_{ID2} provides direct information on recombination behavior and physical insight into the device state. Therefore, the proposed method provides a deeper understanding of the evolution of recombination processes originating from different degradation mechanisms, revealing not just the degradation profile but also how it is produced in terms of recombination pathways. This complementarity is especially interesting for photovoltaic devices whose

outdoor behavior is under study, development and optimization, as is currently the case for perovskite solar cells.

Finally, it should be noted that each technology has its own peculiarities, which often necessitate the revision of characterization methods, and PSCs are no exception. Proof of this is provided by the very recent consensus[16] related to the stability measurement of PSCs. Here, we contribute to this discussion by providing a high-throughput analysis that takes advantage of the peculiarities of perovskite technology for the determination of the outdoor performance of PSCs. Regarding future systematic studies of PSCs operating outdoors, we recommend reporting data collected under the NOCT power rating conditions suggested by IEC 61853-1, which are commonly addressed in datasheets for commercial technologies and are possible to achieve under outdoor test conditions. The complementary analysis and determination of n_{ID} can provide critical information for device characterization and the understanding of degradation processes to accelerate the optimization of this technology or other technologies with similar properties that could be under development.

Methods

Monitoring system. The monitoring system used in this study includes electronic analyzers for measuring I-V curves and a data management system for storing, synchronizing and processing electrical and weather records[25]. The irradiance levels were measured using a Spektron 210 sensor (TRITEC International). Moreover, we considered the NOCT conditions defined in the IEC 61853-1 standard, corresponding to ambient temperature and an irradiance of 800 W/m^2, and the ambient temperature was recorded using PT-1000 sensors (TRITEC International). To simplify the methodology, the ambient temperature was used in the various calculations, as it presents a trend similar to that of the module temperature, this approach introduces a relative error lower than 5% (**Supplementary Figure 17**). Further discussion on the relation between the ambient temperature and the temperature of a perovskite device can be found elsewhere[4]. Moreover, the devices were evaluated at the Universidad de Antioquia (6° 15′ 38″ N 75° 34′ 05″W), facing south at a fixed angle of 10°. Weather data (irradiance and ambient temperature) and electrical data (I-V curves) were recorded every minute during daylight hours (5:30 am to 6:30 pm). The methods and equipment used have been discussed and explained in previous work[4,25,36]. A brief description of the methods used to process the data is provided in **Supplementary Figure 3**. The electrical and weather data were synchronized at the remote server using the timestamp of each record, creating a database including date, time, irradiance, temperatures, and data extracted from the I-V curves, such as V_{oc}, I_{sc}, FF, P_{max} and efficiency. Then, to minimize the influence of atypical data or data related to unclear days, shadowing, dirt or droplets on

the surface, a linearity determination criterion was applied based on the linear behavior observed between P_{max} and the irradiance and validated by a high coefficient of determination (r-value) close to 1 (**Supplementary Figure 4a**). In this way, the best-fit data with a deviation of ±5% were selected as the filtered data, which were taken to represent the average conditions during the exposure time. The outdoor performance, power rating conditions and n_{ID} results were calculated using these filtered data in accordance with the flowchart describe in **Supplementary Note 1 and Note 2**. ~~The experimental data collected in the outdoor test and used in this work are available from the web site: http://elektra.udea.edu.co/solarudea/.~~

Indoor measurements. To obtain the n_{ID} value indoors, we used an LED lamp. The light intensities were controlled using an optical filter from Thorlabs. To measure the impedance frequency and V_{oc} at each intensity, an Autolab procedure was developed (see **Supplementary Note 3~~2~~**). In this procedure, V_{oc} was recorded for 1 minute, and the average value was taken as the V_{oc} value corresponding to that light intensity. Subsequently, the bias of a potentiostat was set to $V_{oc,}$ and impedance/frequency-response analysis was performed in the range of 100 mHz and 1 MHz, using an AC signal of 10 mV in amplitude and scanning first from high to low frequency (down) and then from low to high frequency (up) to ensure the reliability of the measurement while avoiding parasitic effects (**Supplementary Figure 12**). Finally, the I-V curve of the device at 1 sun was recorded. All experiments were performed at room temperature (approximately 25°C). On the other hand, the impedance/frequency-response data were fitted considering the equivalent circuit, as reported elsewhere[48] and shown in **Supplementary Figure 13**, to estimate the parameters. For impedance fitting, a global optimization process involving a genetic algorithm (GA) and the simplex method was used, as reported in a previous work[33], to minimize the square error between the measured impedance (Z) and the impedance calculated using the equivalent circuit (Z_{model}) at the frequencies considered (f), considering all samples recorded (NS) (**Eq. (3)**). The main parameters of the genetic algorithm used to perform the optimization process were a randomly initialized population with a size of 200, tournament selection, a two-point crossover function, uniform mutation and 600 generations as the stopping criterion. After that, the GA finds the solution, which is used as the initial condition in the Simplex method to improve the error.

$$Error = \sqrt{\sum_{k=1}^{NS}\left(Z(f(k)) - Z_{model}(R_s, L_s, R_b, C_b, C_{g,}R_{rec}, f(k))\right)^2} \quad (3)$$

Device fabrication. Minimodules were fabricated with an inverted structure of ITO/NiO_x/Al_2O_3/$MAPbI_3$/PCMB/rhodamine/Au, which has been demonstrated to be feasible for the fabrication of large-area devices up to 100 cm^2 [4,36]. However, in this work, we used an ITO substrate of 5 x 5 cm with 4 cells interconnected in series, each with an of active area of approximately 2 cm^2 (see **Fig. 1**, **Supplementary Figure 1 and Supplementary Table 1**), to produce more samples for evaluation. In this structure, the incorporation of the NiO_x and the mesoporous layer (Al_2O_3) improves the reproducibility for fabrication over large areas and reduces hysteresis[50,51], while the incorporation of rhodamine improves the electronic effects[52]. Moreover, the perovskite $MAPbI_3$ was obtained by dissolving the precursor in acetonitrile/methylamine. The full characterization of the $MAPbI_3$ layer, which included a solvent treatment with methyl ammonium chloride and the creation of scribe lines (P1, P2 and P3), has been reported in previous work[36]. Finally, the devices were manually encapsulated with ethylene vinyl acetate (EVA), and the borders were covered with epoxy resin to minimize the direct exposure of the EVA.

Acknowledgments

Esteban Velilla thanks Colombia's Administrative Department of Science, Technology and Innovation (COLCIENCIAS) for national doctoral scholarship number 727-2015 (contract No. FP44842-124-2017). The authors gratefully acknowledge the financial support provided by the Colombia Scientific Program within the framework of the call Ecosistema Científico (Contract No. FP44842- 218-2018) and by the European Research Council (ERC) via a Consolidator Grant (724424 - No-LIMIT).

Author contributions

E.V. fabricated, installed, monitored and characterized the minimodules under indoor and outdoor conditions and processed and analyzed the data. F.J. directed the device fabrication and data collection. I.M.-S. designed and directed the data analysis. All authors participated in the discussion and interpretation of the results and the preparation of the manuscript.

Competing interests

The authors declare no competing interests.

Data availability statement

All data generated or analyzed during this study are included in the published article and its Supplementary Information and Source Data files. All experimental data collected in the outdoor test and used in this work have been gathered in an open data repository at the University of Antioquia and are available at the following web site: http://elektra.udea.edu.co/solarudea/. In this way, to reproduce the results of this work, weather data and data extracted from the I-V curves, were processed in accordance with the flowchart shown in **Supplementary Figure 3**.

References

1. Makrides, G., Zinsser, B., Schubert, M. & Georghiou, G. E. Performance loss rate of twelve photovoltaic technologies under field conditions using statistical techniques. *Sol. Energy* **103**, 28–42 (2014).
2. Phinikarides, A., Kindyni, N., Makrides, G. & Georghiou, G. E. Review of photovoltaic degradation rate methodologies. *Renew. Sustain. Energy Rev.* **40**, 143–152 (2014).
3. Hu, Y. *et al.* Standardizing Perovskite Solar Modules beyond Cells. *Joule* **3**, 2076–2085 (2019).
4. Velilla, E., Ramirez, D., Uribe, J.-I., Montoya, J. F. & Jaramillo, F. Outdoor performance of perovskite solar technology: Silicon comparison and competitive advantages at different irradiances. *Sol. Energy Mater. Sol. Cells* **191**, 15–20 (2019).
5. Tress, W. *et al.* Performance of perovskite solar cells under simulated temperature-illumination real-world operating conditions. *Nat. Energy* **4**, 568–574 (2019).
6. Deng, Y. *et al.* Tailoring solvent coordination for high-speed, room-temperature blading of perovskite photovoltaic films. *Sci. Adv.* **5**, eaax7537 (2019).
7. Green, M. A., Blakers, A. W. & Osterwald, C. R. Characterization of high- efficiency silicon solar cells. *J. Appl. Phys.* **58**, 4402–4408 (1985).
8. Osterwald, C. R., Glatfelter, T. & Burdick, J. Comparison of the temperature coefficients of the basic I-V parameters for various types of solar cells. in *Conference Record of the IEEE Photovoltaic Specialists Conference* 188–193 (1987).
9. Hasan, O. & Arif, A. F. M. Performance and life prediction model for photovoltaic modules: Effect of encapsulant constitutive behavior. *Sol. Energy Mater. Sol. Cells* **122**, 75–87 (2014).
10. Wang, E., Yang, H. E., Yen, J., Chi, S. & Wang, C. Failure modes evaluation of PV module via materials degradation approach. *Energy Procedia* **33**, 256–264 (2013).
11. Oliveira, M. C. C. de, Diniz Cardoso, A. S. A., Viana, M. M. & Lins, V. de F. C. The causes and effects of degradation of encapsulant ethylene vinyl acetate copolymer (EVA) in crystalline silicon photovoltaic modules: A review. *Renew. Sustain. Energy Rev.* **81**, 2299–2317 (2018).

12. Osterwald, C. R. & McMahon, T. J. History of accelerated and qualification testing of terrestrial photovoltaic modules: A literature review. *Prog. Photovoltaics Res. Appl.* **17**, 11–33 (2009).
13. Holzhey, P. & Saliba, M. A full overview of international standards assessing the long-term stability of perovskite solar cells. *J. Mater. Chem. A* **6**, 21794–21808 (2018).
14. Anoop, K. M. *et al.* Bias- Dependent Stability of Perovskite Solar Cells Studied Using Natural and Concentrated Sunlight. *Sol. RRL* **4**, 1900335 (2020).
15. Yang, J., Siempelkamp, B. D., Liu, D. & Kelly, T. L. Investigation of $CH_3NH_3PbI_3$ Degradation Rates and Mechanisms in Controlled Humidity Environments Using in Situ Techniques. *ACS Nano* **9**, 1955–1963 (2015).
16. Domanski, K., Alharbi, E. A., Hagfeldt, A., Grätzel, M. & Tress, W. Systematic investigation of the impact of operation conditions on the degradation behaviour of perovskite solar cells. *Nat. Energy* **3**, 61–67 (2018).
17. Cheacharoen, R. *et al.* Design and understanding of encapsulated perovskite solar cells to withstand temperature cycling. *Energy Environ. Sci.* **11**, 144–150 (2018).
18. Khenkin, M. V. *et al.* Consensus statement for stability assessment and reporting for perovskite photovoltaics based on ISOS procedures. *Nat. Energy* **5**, 35–49 (2020).
19. Domanski, K. *et al.* Migration of cations induces reversible performance losses over day/night cycling in perovskite solar cells. *Energy Environ. Sci.* **10**, 604–613 (2017).
20. Khenkin, M. V. *et al.* Reconsidering figures of merit for performance and stability of perovskite photovoltaics. *Energy Environ. Sci.* **11**, 739–743 (2018).
21. Christians, J. A., Manser, J. S. & Kamat, P. V. Best practices in perovskite solar cell efficiency measurements. Avoiding the error of Making Bad Cells Look Good. *Journal of Physical Chemistry Letters* **6**, 852–857 (2015).
22. Schwenzer, J. A. *et al.* Temperature Variation-Induced Performance Decline of Perovskite Solar Cells. *ACS Appl. Mater. Interfaces* **10**, 16390–16399 (2018).
23. Hoye, R. L. Z. *et al.* Perovskite-Inspired Photovoltaic Materials: Toward Best Practices in Materials Characterization and Calculations. *Chem. Mater.* **29**, 1964–1988 (2017).
24. Wang, M. *et al.* Evaluation of Photovoltaic Module Performance Using Novel Data-driven I-V Feature Extraction and Suns-V_{OC} Determined from Outdoor Time-Series I-V Curves. in *2018 IEEE 7th World Conference on Photovoltaic Energy Conversion, WCPEC 2018 - A Joint Conference of 45th IEEE PVSC, 28th PVSEC and 34th EU PVSEC* 778–783 (IEEE, 2018). doi:10.1109/PVSC.2018.8547772
25. Velilla, E., Cano, J. B. & Jaramillo, F. Monitoring system to evaluate the outdoor performance

of solar devices considering the power rating conditions. *Sol. Energy* **194**, 79–85 (2019).

26. Tress, W. *et al.* Interpretation and evolution of open-circuit voltage, recombination, ideality factor and subgap defect states during reversible light-soaking and irreversible degradation of perovskite solar cells. *Energy Environ. Sci.* **11**, 151–165 (2018).
27. Kerr, M. J. & Cuevas, A. Generalized analysis of the illumination intensity vs. open-circuit voltage of solar cells. *Sol. Energy* **76**, 263–267 (2004).
28. Santakrus Singh, N., Jain, A. & Kapoor, A. Determination of the solar cell junction ideality factor using special trans function theory (STFT). *Sol. Energy Mater. Sol. Cells* **93**, 1423–1426 (2009).
29. Bashahu, M. & Nkundabakura, P. Review and tests of methods for the determination of the solar cell junction ideality factors. *Sol. Energy* **81**, 856–863 (2007).
30. Contreras-Bernal, L. *et al.* Impedance analysis of perovskite solar cells: A case study. *J. Mater. Chem. A* **7**, 12191–12200 (2019).
31. Almora, O. *et al.* Discerning recombination mechanisms and ideality factors through impedance analysis of high-efficiency perovskite solar cells. *Nano Energy* **48**, 63–72 (2018).
32. Yoo, S.-M. *et al.* Nanoscale Perovskite- Sensitized Solar Cell Revisited: Dye- Cell or Perovskite- Cell? *ChemSusChem* **13**, 2571–2576 (2020).
33. Velilla, E. *et al.* Numerical Analysis to Determine Reliable One-Diode Model Parameters for Perovskite Solar Cells. *Energies* **11**, 1963 (2018).
34. Agarwal, S. *et al.* On the Uniqueness of Ideality Factor and Voltage Exponent of Perovskite-Based Solar Cells. *J. Phys. Chem. Lett.* **5**, 4115–4121 (2014).
35. Dunfield, S. P. *et al.* From Defects to Degradation: A Mechanistic Understanding of Degradation in Perovskite Solar Cell Devices and Modules. *Adv. Energy Mater.* 1904054 (2020). doi:10.1002/aenm.201904054
36. Ramirez, D., Velilla, E., Montoya, J. F. & Jaramillo, F. Mitigating scalability issues of perovskite photovoltaic technology through a p-i-n meso-superstructured solar cell architecture. *Sol. Energy Mater. Sol. Cells* **195**, 191–197 (2019).
37. IEC 61853-1. *Photovoltaic (PV) module performance testing and energy rating - Part 1: Irradiance and temperature performance measurements and power rating*. *International Electrotechnical Committee* (2011).
38. Reese, M. O. *et al.* Consensus stability testing protocols for organic photovoltaic materials and devices. *Sol. Energy Mater. Sol. Cells* **95**, 1253–1267 (2011).
39. Meeker, W., Hong, Y. & Escobar, L. Degradation Models and Analyses. in *Encyclopedia of*

Statistical Sciences (John Wiley & Sons, Inc., 2011). doi:10.1002/0471667196.ess7148

40. He, S., Qiu, L., Ono, L. K. & Qi, Y. How far are we from attaining 10-year lifetime for metal halide perovskite solar cells? *Mater. Sci. Eng. R Reports* **140**, 100545 (2020).
41. Khadka, D. B., Shirai, Y., Yanagida, M. & Miyano, K. Degradation of encapsulated perovskite solar cells driven by deep trap states and interfacial deterioration. *J. Mater. Chem. C* **6**, 162–170 (2018).
42. Ma, C. *et al.* Effects of Small Polar Molecules (MA^+ and H_2O) on Degradation Processes of Perovskite Solar Cells. *ACS Appl. Mater. Interfaces* **9**, 14960–14966 (2017).
43. Lee, H., Lee, C. & Song, H.-J. Influence of Electrical Traps on the Current Density Degradation of Inverted Perovskite Solar Cells. *Materials (Basel).* **12**, 1644 (2019).
44. Stoichkov, V. *et al.* Outdoor performance monitoring of perovskite solar cell mini-modules: Diurnal performance, observance of reversible degradation and variation with climatic performance. *Sol. Energy* **170**, 549–556 (2018).
45. Bisquert, J. & Juarez-Perez, E. J. The Causes of Degradation of Perovskite Solar Cells. *J. Phys. Chem. Lett.* **10**, 5889–5891 (2019).
46. McLeod, J. A. & Liu, L. Prospects for Mitigating Intrinsic Organic Decomposition in Methylammonium Lead Triiodide Perovskite. *J. Phys. Chem. Lett.* **9**, 2411–2417 (2018).
47. Motti, S. G. *et al.* Controlling competing photochemical reactions stabilizes perovskite solar cells. *Nat. Photonics* **13**, 532–539 (2019).
48. Yoo, S.-M. *et al.* An Equivalent Circuit for Perovskite Solar Cell Bridging Sensitized to Thin Film Architectures. *Joule* **3**, 2535–2549 (2019).
49. Fabregat-Santiago, F., Garcia-Belmonte, G., Mora-Seró, I. & Bisquert, J. Characterization of nanostructured hybrid and organic solar cells by impedance spectroscopy. *Phys. Chem. Chem. Phys.* **13**, 9083 (2011).
50. Ramirez, D. *et al.* Meso-Superstructured Perovskite Solar Cells: Revealing the Role of the Mesoporous Layer. *J. Phys. Chem. C* **122**, 21239–21247 (2018).
51. Ciro, J. *et al.* Self-Functionalization Behind a Solution-Processed NiOx Film Used As Hole Transporting Layer for Efficient Perovskite Solar Cells. *ACS Appl. Mater. Interfaces* **9**, 12348–12354 (2017).
52. Ciro, J. *et al.* Optimization of the Ag/PCBM interface by a rhodamine interlayer to enhance the efficiency and stability of perovskite solar cells. *Nanoscale* **9**, 9440–9446 (2017).